PHYSICSAccess Research Paper
ISSN Online: 2756-3898, ISSN Print: 2714-500X https://doi.org/10.47514/phyaccess.2022.2.2.012

Effect of sputtered silver thin film thickness towards morphological and optical properties of black silicon fabricated by two-step silver-assisted wet chemical etching for solar cells application

Auwal Abdulkadir[1], Aliyu K Isiyaku[2], Mustapha Isah[2], Dallatu U Abbas[2] and Tijjani Ismaila[3]

[1] Department of Physics, Umaru Musa Yar'adua University, P. M. B. 2218 Katsina, Nigeria
[2] Department of Physics, Kaduna State University, P.M.B 2339, Kaduna State, Nigeria
[3]Department of Applied Physics, School of Applied Sciences, College of Science and Technology, Kaduna Polytechnic, Kaduna State, Nigeria

Corresponding E-mail: auwal.abdulkadir@umyu.edu.ng

Received 24-10-2022
Accepted for publication 21-11-2022
Published 28-11-2022

Abstract

Effect of sputtered silver (Ag) thin film thickness towards morphological and optical properties of black silicon (b-Si) fabricated by two-step silver-assisted wet chemical etching for solar cells applications is investigated. The method involves low temperature annealing of crystalline silicon (c-Si) coated with Ag thin films of 10 nm, 15 nm, and 25 nm. This is followed by an etching in a solution of HF:H_2O_2:DI H_2O (1:5:10 volume ratio) at room temperature for 70 s. Dense and spherical Ag NPs with an average diameter of 203 ± 17.8 nm and surface coverage of about 72.5% are achieved on a sample with Ag film thickness of 15 nm prior to the annealing process. After the etching, the average nanopores' height of ~420 nm with an average diameter of ~200 nm owing to denser Ag NPs on the c-Si surface before the etching are obtained. Optical absorption enhancement due to low weight average reflection (WAR) within wavelength region of 300–1100 nm is observed on the b-Si wafers. Sample with 15 nm of Ag thin film prior to annealing, demonstrates WAR of 7.7% compared 40.0% of the reference planar c-Si. The low WAR is due to the efficient light coupling effect of the b-Si nanopores. The fabricated b-Si nanopores can be used in b-Si solar cells for enhanced optical absorption and high photocurrent in the future.

Keywords: Silver film thickness; two-step silver assisted etching; black silicon; absorption

I. Introduction

Crystalline silicon (c-Si) possess low absorption coefficient which leads to low light absorption in c-Si solar cells. Also, the c-Si has high surface reflection, which results in about ~40% of the incident light to be reflected at the interface of air and c-Si [1–3]. Surface modification of c-Si via nano texturing (b-Si) is a promising method that can overcome the problem of high surface reflection in c-Si. B-Si nano textured surfaces are achieved through etching process [4]. Due to the presence of the nano-textures resulted from the etching process, surface reflection of the c-Si is reduced in a

broadband range of 300–1100 nm [4-5]. Reduced surface reflection result in an enhanced optical absorption of the solar cells [4-5]. The enhanced light absorption in b-Si is attributed to an enhanced light trapping and coupling by the nano-textures [6].

Numerous techniques have been investigated for the fabrication of b-Si nano-textures [4, 7]. The methods include reactive ion etching (RIE) which was erroneously discovered in 1990s, plasma immersion ion implantation (PII), and laser irradiation (LI) [8, 9]. The afore mentioned techniques involve the requirement of high-tech equipment and more timely processing procedures, which may lead to b-Si solar cells at a high cost per unit watt ($/W). Recently, metal-assisted chemical etching (MACE) has been widely studied. MACE of c-Si is a much more straightforward, promising, and low-cost approach to produce the b-Si [2, 10]. Besides, MACE process does not require high-tech equipment or lengthy processing procedures. MACE process comprises two process steps; surface nucleation of metal catalyst and anisotropic etching which can be classified as electroless and non-electroless MACE. In electroless MACE liquid metal catalysts sources like $AgNO_3$ or $CuSO_4$ are used as the source of metal catalyst. Also, MACE is categorized into one and two-step methods [7]. One-step MACE category utilizes the metal catalyst in $HF:H_2O_2$:DI H_2O aqueous solution and the etching process steps take place simultaneously [8-10]. Nano-textures fabricated by one-step MACE are usually with 2-10 µm height, which lead to low broadband reflection but demonstrate high surface recombination in the b-Si solar cells [10]. In two-step MACE category, the metal catalysts are deposited either in aqueous solution (electroless) or via thermal evaporation or sputtering (non-electroless), followed by subsequent etching in $HF:H_2O_2$ solution [11, 12].

The most used catalysts for MACE include silver (Ag), gold (Au) and copper (Cu). B-Si solar cells fabricated with b-Si produced using Au and Cu-based metal catalysts suffer from high electron and hole charge carrier recombination losses [13-16]. The high charge carrier recombination originates from the Au or Cu metal traces which acts as recombination sites in the b-Si solar cells [15, 16]. In this paper, Ag metal is chosen as a catalyst for the consideration of lower recombination losses in the future b-Si solar cells. Reference [17] investigated the fabrication of nano-textures on c-Si and nano-hole array by non-electroless two step MACE method using Ag catalyst, where a thin layer of Ag was thermally evaporated on silicon wafers and then annealed at low temperature for 10 min. The samples were then etched for 5-20 min duration, and nano-textures with lengths range of 0.5–2 µm were obtained. However, no optical results presented. Reference [18] studied the effects of Ag NPs' diameter and percentage coverage on b-Si formation in electroless two-step MACE process. This was done by alternating the Ag NPs deposition time prior to etching. In their work, it was observed that the density of b-Si nanowire arrays decreases with the increase in Ag NPs deposition. Recently, [19] investigated the role of Ag NPs morphology and $AgNO_3$ molarity on the size of b-Si nanowires produced by electroless two-step MACE. From their findings, it was demonstrated that the Ag NPs diameter and surface density increased with deposition time and larger Ag NPs were formed with longer deposition time, which adversely affect the morphology of the b-Si nanowires. To best of our knowledge, there has been no reported work addressing the effects of Ag NPs catalysts morphology towards morphological and optical properties of b-Si nano-textures produced by non-electroless two-step MACE process. In our previous study, we investigated the effects of Ag nanoparticles (NPs) layer thickness towards optical and morphological properties of b-Si fabricated by electroless two-step MACE for photovoltaics [20]. It is equally important to investigate the effects of Ag NPs morphology resulted from Ag thin film of different thickness towards properties of b-Si nano-textures produced by non-electroless Ag-based two-step MACE process.

This paper investigates the effect of Ag catalyst surface morphology on fabrication of b-Si via a non-electroless two-step MACE method. The process utilizes Ag NPs produced from deposition of Ag thin films with different thicknesses; 10, 15, and 25 nm by RF sputtering. A low temperature annealing of 240 ℃ for 40 min follows the Ag thin film deposition step to form Ag NPs. The annealed c-Si wafers with the formed Ag NPs are then etched in aqueous solution of $HF:H_2O_2$:DI H_2O (1:5:10 volume ratio) at room temperature for 70 s to form b-Si nano-textures. The effects of the Ag NPs catalysts morphology towards surface morphological and optical properties of the b-Si are then investigated and analyzed.

II. Materials and Methods

A. Fabrication of b-Si nano-textures

Fabrication of b-Si utilizes substrates of p-type mono-crystalline silicon (250 µm-thick) wafers with 1–10 Ω cm resistivity. The wafers are cleaned using Radio Corporation of America (RCA) technique to remove contaminations [18]. Native oxide is removed by a short dip in $HF:H_2O$ solution. For fabrication of b-Si surfaces, 10, 15, and 25 nm of Ag thin films are deposited on c-Si wafers by RF sputtering at base pressure of 4×10^{-5} $Torr$. The wafers are then annealed at 240 ℃ in a furnace for 40 min under N_2 ambient at flow rate of 2 L/min [21]. After the annealing process, Ag NPs are formed on the wafers. The wafers are then etched in an aqueous solution of HF (50%):H_2O_2 (30%): DI H2O (1:5:10 volume ratio) [21] at room temperature for 70 s. After the etching process, residual Ag NPs are removed using concentrated HNO_3 (60%) in a sonification bath for few minutes. The etched c-Si wafers are then dipped again in HF solution for a brief duration to remove native oxide.

B. Characterization of b-Si

Field Emission Scanning Electron Microscopy (FESEM) (Model: FEI Nova NanoSEM 450) was used to characterize

the surface morphologies of the annealed Ag NPs resulted from different film thicknesses of Ag and b-Si wafers. FESEM was also used to characterize the top view of the annealed c-Si wafers with deposited Ag NPs of different morphologies, top view, and cross section of the b-Si nano-textures. The top view FESEM images are then analyzed by Image J software. Atomic Force Microscopy (AFM) (Model: Dimension Edge, Bruker) was further used to characterize the surface morphologies of the b-Si wafers. The height and root mean square (RMS) surface roughness of the b-Si wafers are obtained from the AFM analysis. Scan range of $10\ \mu m \times 10\ \mu m$ and resolution of 512 pixels were used during the analysis. For optical characterizations, reflection (R) and transmission (T) curves of the b-Si wafers are measured by Agilent Cary 5000 UV–Vis–NIR spectrophotometer (equipped with an integrating sphere) within $300-1100\ nm$ spectral region. From the reflection results, average weighted reflection (WAR) is calculated within the same wavelength region using Equation (1). From the reflection and transmission curves, absorption (A) is then calculated as A = (100–R–T) % [20, 21]. Slight hysteresis in some of the reflection and absorption curves at 800 nm is due to detector switching during taking measurements from the UV–Vis–NIR spectrophotometer.

$$WAR = \frac{\int_{300\ nm}^{1100\ nm} R(\lambda)S(\lambda)d\lambda}{\int_{300\ nm}^{1100\ nm} S(\lambda)d\lambda} \quad (1)$$

III. RESULTS AND DISCUSSIONS

Fig. 1 illustrates the images of c-Si wafers decorated with Ag NPs produced after the annealing process.

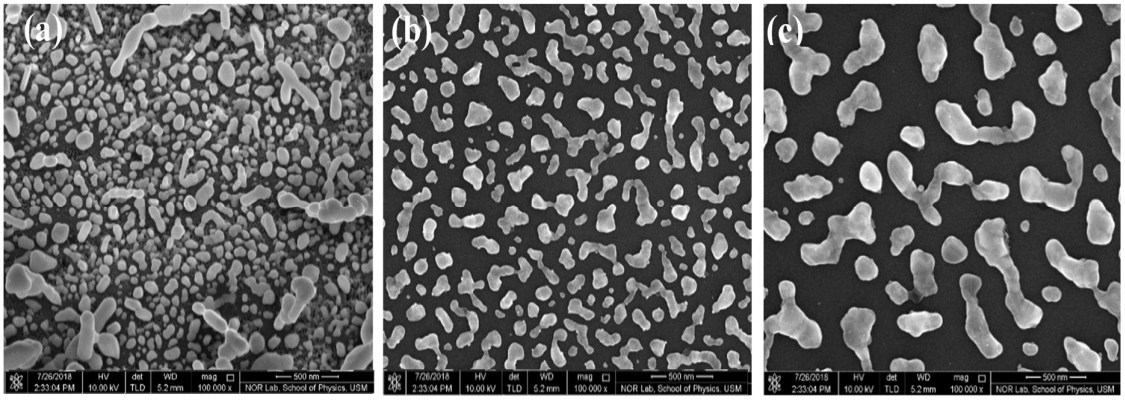

Fig. 1 30° tilt top view FESEM images of wafers with Ag NPs formed after annealing c-Si with Ag thin films of different thicknesses at 240°C for 40 min under N_2; (a) 10 nm (b) 15 nm and (c) 25 nm. The scale bar represents 500 nm.

The wafers with Ag thin film thicknesses of 10, 15, and 25 nm were subjected to a moderate temperature annealing at 240°C for 40 min under 2 L/min of N_2 gas. From the images, it is evident that the c-Si wafers appear to have Ag NPs of different sizes and morphology owing to possession of Ag thin film with different thicknesses prior to the annealing process. The c-Si wafer with 10 nm (Fig. 1 (a)) of Ag thin film appears to have Ag NPs with smaller diameters. The diameter sizes of the Ag NPs range between 50-70 nm with a surface coverage of about 80% as revealed by the image J software. For a selected area, an average diameter size of 55 ± 3 nm was obtained. Besides, some bigger Ag NPs appears on the sample's surface. This may arise due to conjunction of near-by Ag NPs to form bigger Ag NPs. Conjunction of Ag NPs occurs due to smaller feature sizes of the NPs produced from a lower Ag thin film of 10 nm [21, 22]. The c-Si wafer with 15 nm (Fig. 1 (b)) of Ag thin film prior to the annealing appears to have dense, spherical, and slightly bigger Ag NPs with sizes of around 70-200 nm and surface coverage of about 72.5% after the annealing process. The image J software analysis revealed an average diameter size of 203 ± 17.8 nm. Conjunction of near-by Ag NPs is precisely negligible for this sample. For the sample with Ag thin film of 25 nm before the annealing process, bigger Ag NPs with diameter range of 100-370 nm were obtained after the annealing. The image J software shows an average diameter size of 350 ± 7.9 nm. For this sample, Ag+ migrates to energetically favored sites (sites with already grown nuclei of Ag NPs instead on bare c-Si) and Ag NPs appear slightly as bigger dendrites with average diameter of ~350 nm. This is the reason of the observed slight decrease in Ag NPs density, surface coverage (to about 60%) and increased inter-particle distances between Ag NPs as reported by similar findings [21-23].

To understand the impact of Ag NPs with different morphology on surface morphology of the b-Si wafers due to the presence of different Ag thin film thickness prior to the annealing process, subsequent etching in an aqueous solution of HF:H_2O_2 was employed. Images of the fabricated b-Si samples are shown in Fig. 2. When subsequent immersion of c-Si wafers deposited with Ag NPs into an aqueous etching solution of HF:H_2O_2:DI H_2O (1:5:10) is employed for 70 s,

uniform H_2O_2-aided HF etching results from continuous galvanic displacement of c-Si via the formation of many local nano-electrochemical cells having reactions at cathode and anode, with Ag NPs acting as the catalyst. Details on the etching mechanism can be found in related literatures [12, 24]. Briefly, the b-Si formation mechanism is based on dual role of Ag NPs (i.e., surface protection and etching catalytic role). Electron exchange between c-Si and Ag NPs is responsible for Ag NPs sinking into the c-Si bulk when an Ag NPs deposited c-Si wafer was immersed in the etching solution [12, 24]. Fig. 2 illustrates the images of b-Si wafers formed after etching the c-Si decorated with Ag NPs of different morphology resulted from Ag thin films of different thicknesses. In accordance with Fig. 1, the etched wafers appear to possess nano-pores of different average diameters 60 nm, 200 nm, and 350 nm for the etched wafers with 10 nm (Fig. 2 (a)), 15 nm (Fig. 2 (b)), and 25 nm (Fig. 2 (c)) of Ag thin film prior to the annealing process. Image J analysis reveals that the diameters of the etched b-Si samples are clear projection of the Ag NPs diameters observed in Fig. 1. This is because the nano-pores diameters are outline of the Ag NPs [23-25].

Electron exchange between c-Si and Ag NPs is responsible for Ag NPs sinking into the c-Si bulk when an Ag NPs deposited c-Si wafer was immersed in the etching solution [12, 24, 25]. Fig. 2 illustrates the images of b-Si wafers formed after etching the c-Si decorated with Ag NPs of different morphology resulted from Ag thin films of different thicknesses. In accordance with Fig. 1, the etched wafers appear to possess nano-pores of different average diameters 60 nm, 200 nm, and 350 nm for the etched wafers with 10 nm (Fig. 2 (a)), 15 nm (Fig. 2 (b)), and 25 nm (Fig. 2 (c)) of Ag thin film prior to the annealing process. Image J analysis reveals that the diameters of the etched b-Si samples are clear projection of the Ag NPs diameters observed in Fig. 1. This is because the nano-pores diameters are outline of the Ag NPs [21-26].

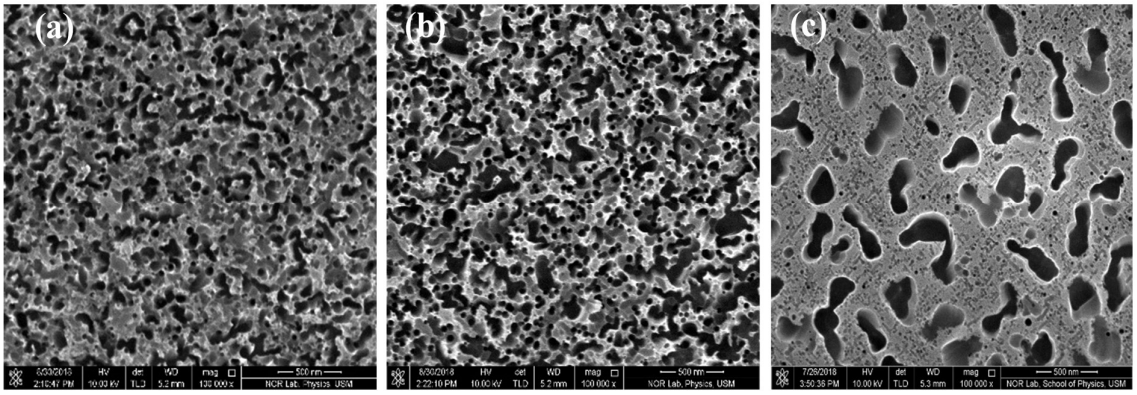

Fig. 2 30° tilt top view FESEM images of b-Si wafers formed after etching c-Si with Ag NPs of different morphology resulted from Ag thin films of different thicknesses; (a) 10 nm (b) 15 nm and (c) 25 nm. The scale bar represents 500 nm.

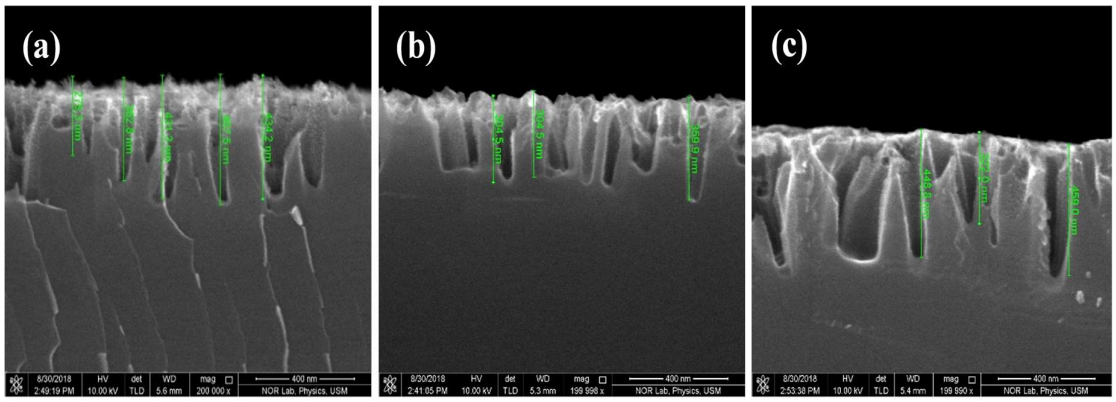

Fig. 3 Cross section FESEM images of b-Si wafers formed after etching c-Si with Ag NPs of different morphology resulted from Ag thin films of different thicknesses; (a) 10 nm (b) 15 nm and (c) 25 nm. The scale bar represents 400 nm.

To get better understanding of the surface morphology of the b-Si nano-pores, cross-sectional FESEM images are illustrated in Fig. 3. The nano-pores possess height of 300-420 nm and diameter of 100-300 nm which agree with the average diameter extracted from ImageJ analysis presented earlier. When the wafer with 10 nm Ag thin film prior to annealing is etched for 70 s (Fig. 3(a)), nano-pores with varying heights between 323-450 nm and an averaged diameter of ~105 nm is evident. When the sample with 15 nm Ag thin film prior to annealing is etched (Fig. 3 (b)), the height of the nano-pores maintain a precise and uniform increase to an average value of 420 nm. Slight increase in the average diameter to about ~200 nm is observed. This is in accordance with the observation presented in Fig 2 (b) earlier. When the wafer sample with Ag thin film of 25 nm prior to the annealing is etched (Fig 3 (c)), the nano-pores heights slightly reduced to a varying value of around 350-410 nm with an average diameter of about ~320 nm. For this sample, majority of the base diameters appear to be square-like. This is believed to be due to enhanced lateral etching process due to bigger Ag NPs with larger diameters. Lateral etching prefers to occur along the direction of Si-Si bonding due to possession of higher free energy. Thus, for sample with bigger Ag NPs, lateral etching is also favored instead of etching underneath Ag NPs alone [20, 27]. The cross-sectional FESEM images indicate that the height of the b-Si nano-pores and diameters are both tunable by adjusting the Ag thin film thickness prior to the annealing process.

Fig. 4 shows 3D AFM images of b-Si nano-pores produced after etching c-Si wafers with Ag NPs of different morphology resulted from Ag thin films of different thicknesses; (a) 10 nm (b) 15 nm and (c) 25 nm. It is evident that the textured c-Si surfaces are characterized by random and dense nano-pores as previously illustrated in the FESEM images of Fig. 3. The height and lateral width of the nano-pores increase with increasing Ag thin film thickness between 10-15 nm. Besides, RMS roughness of the b-Si nano-pores exhibits an increasing trend for c-Si wafers with 10 nm and 15 nm of Ag thin film. The RMS roughness slightly decrease in consistence with the FESEM observations (Fig. 3 (c)) after increasing the Ag thin film to 25 nm. The root mean square (RMS) roughness values are 15.0 nm, 31.0 nm, and 23.8 nm for samples with Ag thin film of 10 nm, 15 nm, and 25 nm prior to the annealing process respectively.

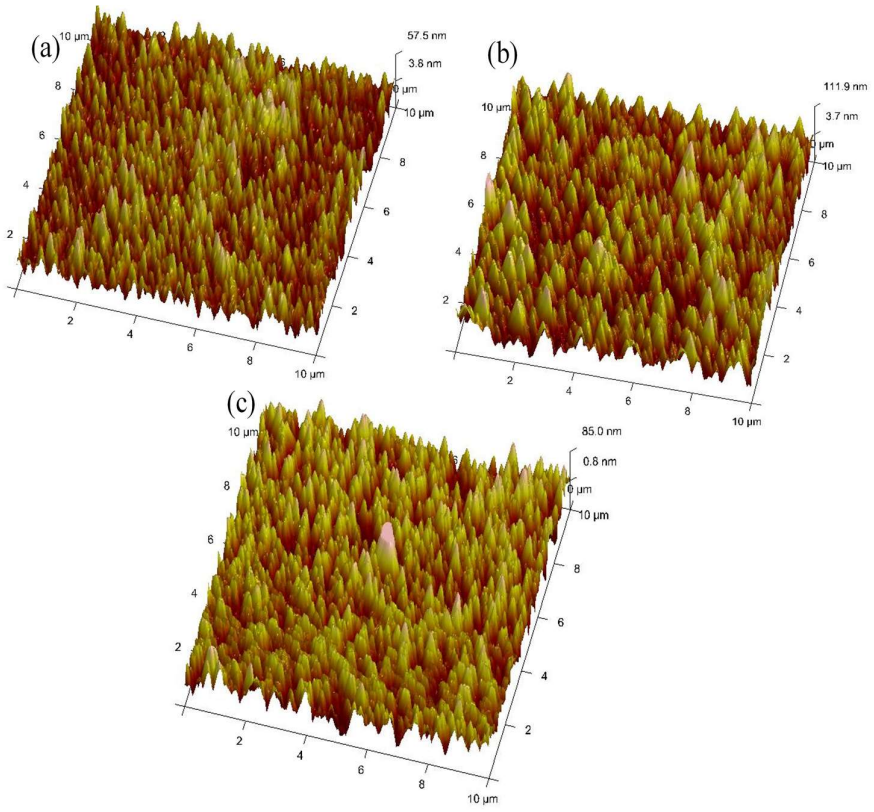

Fig. 4 3D AFM images of b-Si wafers formed after etching c-Si with Ag NPs of different morphology resulted from Ag thin films of different thicknesses; (a) 10 nm (b) 15 nm and (c) 25 nm.

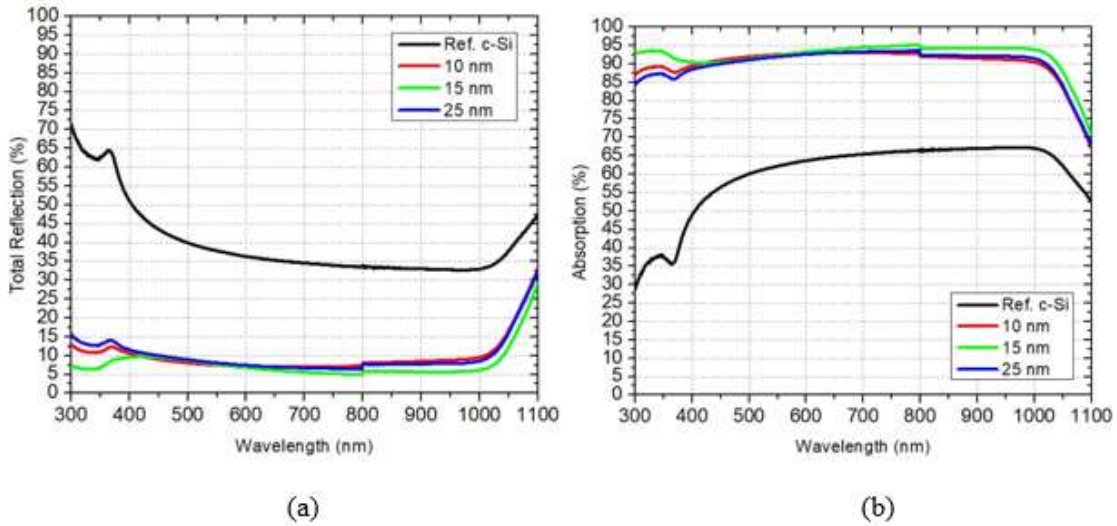

Fig. 5 (a) Total reflection and (b) Absorption of b-Si wafers formed after etching c-Si with Ag NPs of different morphology resulted from Ag thin films of different thicknesses; 10 nm, 15 nm, and 25 nm.

Fig. 5 (a) and (b) reveal the reflection and absorption curves of b-Si nano-pores within wavelength range of $300-1100\ nm$ resulted from different Ag thin thicknesses. Reflection and absorption curves for reference c-Si are shown for comparison. C-Si reference demonstrates high reflection throughout the $300-1100\ nm$ spectral region (WAR of ~40.0 %). The reflection is 39.8 % at wavelength of $600\ nm$. The value of reflection at wavelength of 600 nm is of interest since it represents the peak power of the AM1.5 solar spectrum [21, 27 and 28]. From the figure, a significant reduction of reflection for b-Si across all annealing temperatures is evident. This is due to refractive index (η) grading effect which results in an enhanced light coupling by the b-Si nano-pores [21, 23]. The reflection of the b-Si formed with Ag film thickness of 10 nm drops from 39.8 % to about 8.0% at 600 nm. This leads to absorption of about 92.0% at the same wavelength. This Ag film thickness presents a WAR of 9.7%. Sample with Ag film thickness of 15 nm prior to annealing, shows a reduced broadband ($300-1100\ nm$ wavelength region) reflection. The WAR reduces to 7.7 %. This is attributed to efficient light coupling by the nano-pores with precise uniform average height of 420 nm and average diameter of ~200 nm. For sample with Ag film thickness of 25 nm, the reflection slightly increases to 8.9% at 600 nm. The WAR of 9.8% was obtained for this sample. The b-Si sample with Ag film thickness of 15 nm shows the highest optical absorption throughout the whole spectral range. This owes to the presence of precise and uniform b-Si nano-pores on the c-Si surface which is contributed by the size of Ag NPs of ~200 nm before the etching process. Optimum absorption of ~92.0% has been recorded for the sample. The enhanced light absorption is because of the n grading effect at the air-c-Si interface, owing to the presence of the nanowires [29-31]. When the light is incident on the surface with b-Si nano-pores, the surface appears as a homogenous medium whose η changes gradually from the refractive index of air $(\eta = 1)$ to refractive index of the bulk c-Si $(\eta = 3.8)$. This reduces broadband reflection from the surface [31]. The realized enhanced absorption is applicable in the fabrication of b-Si solar cells where it is translated to high short-circuit current density $(J_{sc(max)})$ of the solar cells.

IV. Conclusion

In this work, b-Si nano-pores are fabricated by a two-step MACE method which combines low temperature annealing of c-Si deposited with Ag thin films with different thicknesses. The method adopts a short etching duration. The Ag NPs are formed from RF sputtering of $10, 15,$ and $25\ nm$ of Ag thin film. The c-Si wafers with the Ag NPs are then etched in aqueous solution of HF:H_2O_2:DI H_2O at room temperature to form b-Si nano-pores. The effects of Ag thin film thickness prior to annealing towards surface morphological and optical properties of the b-Si are then investigated. For Ag thin film of $10\ nm$ prior to annealing, Ag NPs with smaller diameters were formed. The diameter sizes of the Ag NPs ranges between 50-70 nm with a surface coverage of about 80% and average value of $55 \pm 3\ nm$. After the etching, the nano-pores follow the shape of the Ag NPs. Nano-pores with varying heights of $323 - 450\ nm$ and an averaged diameter of $\sim 105\ nm$ is evident. With Ag film thickness of $15\ nm$ prior to annealing, dense, spherical, and slightly bigger Ag NPs with sizes of around $70 - 200\ nm$ and surface coverage of about 72.5 % are formed. Ag NPs with an average diameter size of $203 \pm 17.8\ nm$ is produced. After the etching, the height of the nano-pores maintain a precise and uniform increased height of about $420\ nm$. Slight increase in the average diameter to about $\sim 200\ nm$ is also observed. This is

due to the presence of denser Ag NPs on the surface before the etching. For sample with Ag thin film thickness of 25 nm prior to annealing process, the Ag NPs are less dense on the surface. With this, the nanopores show bigger diameter with range of $100 - 370\ nm$. An average diameter size of $350 \pm 7.9\ nm$ is recorded for the sample. For this sample, Ag^+ migrates to energetically favored sites (sites with already grown nuclei of Ag NPs instead on bare c-Si) and Ag NPs appear slightly as bigger dendrites with average diameter of $\sim 350\ nm$. The surface coverage reduces to about 60% and increased inter-particle distances between Ag NPs was evident. A significant broadband reflection reduction within wavelength region of $300 - 1100\ nm$ is observed on the b-Si wafers with nanopores. Reduction in broadband reflection is reflected as enhanced optical absorption. The reflection of the b-Si with $10\ nm$ of Ag thin film prior to annealing drops to 8.0 % at $600\ nm$ with a corresponding WAR of 9.7 %. With $15\ nm$ of A g thin film prior to annealing, the WAR reduces to the lowest minimum level of 7.7 %, owing to the efficient light coupling effect by the b-Si nano-pores with precisely uniform average height. From the cross-sectional FESEM result, the b-Si nano-pores are dense, precise, uniform, and similar on the surface and have average height of about $420\ nm$. For sample with $25\ nm$ of Ag thin film prior to annealing, the reflection reduces only to 8.9 % at $600\ nm$ due to the sparse formation of the Ag NPs and sparse b-Si nanopores on the c-Si surface after the etching process. In this work, the optimized Ag film thickness prior to annealing for the two-step MACE process is 15 nm of Ag. This film thickness can be used to fabricate b-Si nano-pores for optimum optical absorption and application in b-Si solar cells to achieve high photocurrent in the future.

ACKNOWLEDGMENT

The authors acknowledge Umaru Musa Yar'adua University Katsina, Kaduna State University Kaduna, and TetFund Nigeria for supporting this research.

References

[1] ITRPV, Trends & Challenges in c-Si PV, Photovoltaic Roadmap (ITRPV): 11th Ed., 2022, pp. 1–3 [Online]. Available: https://itrpv.vdma.org/

[2] A. K. Behera, R. N. Viswanath, C. Lakshmanan, K .K. Madapu, M. Kamruddin and T. Mathews, "Synthesis, microstructure and visible luminescence properties of vertically aligned lightly doped porous silicon nanowalls". Microporous Mesoporous Mater, vol. 273 pp. 99–106, 2019.

[3] K. Chen, Y. Liu, X. Wang, L. Zhang and X. Su, "Novel texturing process for diamond-wire-sawn single-crystalline silicon solar cell". Sol. Energy Mater. Sol. Cells, vol. 133, pp. 148–155, 2015.

[4] Y. Fan, P. Han, P. Liang, Y. Xing, Z. Ye and S. Hu, "Differences in etching characteristics of TMAH and KOH on preparing inverted pyramids for silicon solar cells". Appl. Surf. Sci., vol. 264, pp. 761–766, 2013.

[5] H. Zhong, A. Guo, G. Guo, W. Li and Y. Jiang, "The enhanced light absorptance and device application of nanostructured black silicon fabricated by metal-assisted chemical etching". Nanoscale Res. Lett., vol. 11, no. 322, pp. 1-6, 2016.

[6] L. He, C. Jiang, H. Wang, D. Lai, Y. Heng Tan and C. Seng Tan, Rusli, "Effects of nanowire texturing on the performance of Si/organic hybrid solar cells fabricated with a 2.2 μm thin-film Si absorber". Appl. Phys. Lett., vol. 100, pp. 1–5, 2012.

[7] T. P. Pasanen, V. Vähänissi, F. Wolny, A. Oehlke, M. Wagner, M. A. Juntunen, I. T. S. Heikkinen, E. Salmi, S. Sneck, H. Vahlman, A. Tolvanen, J. Hyvärinen and H. Savin, "Industrial applicability of antireflection-coating-free black silicon on PERC solar cells and modules". 35th Eur. Photovolt. Sol. Energy Conf. Exhib., pp. 552–556, 2018.

[8] K. Chen, J. Zha, F. Hu, X. Ye, S. Zou, V. Vähänissi, J.M. Pearce, H. Savin and X. Su, "MACE nano-texture process applicable for both single- and multi-crystalline diamond-wire sawn Si solar cells", Sol. Energy Mater. Sol. Cells, vol. 191, pp. 1–8, 2019.

[9] X. Guo, S. Li, Z. Lei, R. Liu, L. Li, L. Wang, L. Dong, K. Peng and Z. Wang, "Controllable patterning of hybrid silicon nanowire and nanohole arrays by laser interference lithography:. Phys. Status Solidi - Rapid Res. Lett., vol. 14, pp. 1–5, 2020.

[10] W. hadibrata, F. Es, S. Yerci and R. Turan, "Ultrathin silicon solar cell with nanotextured light trapping by metal assisted etching". Sol. Energy Mater. Sol. Cells, vol. 180, pp. 247-252, 2018.

[11] P. Zhang, H. Sun, K. Tao, R. Jia, G. Su, X. Dai, Z Jin and X. Liu, "An 18.9% efficient black silicon solar cell achieved through control of pretreatment of Ag/Cu MACE". J. of Mat. Sci.: Mat. in Elect., vol. 30, pp. 8667-8675, 2019.

[12] R. Tong, W. Zhang, X. Ke, D. Liu and Z. Zhang, "Influence of surface structure on the performance of mono-like Si PERC solar cell". Mat. Sci. Semicond. Proc., vol. 126, no. 105662, pp. 1-7, 2021.

[13] A. A. Leonardi, M. J. Lo Faro and A. Irrera, "CMOS-compatible and low-cost thin film MACE approach for light-emitting Si NWs fabrication". Nanomat., vol. 10, no. 966, pp. 1–11, 2020.

[14] F. Es, E.H. Ciftpinar, O. Demircioglu, M. Gunoven, M. Kulakci and R. Turan, "Performance of solar cells fabricated on black multicrystalline Si by nanowire decoration". Appl. Surf. Sci., vol. 332, pp. 266–271, 2015.

[15] A. K. Isiyaku, A. H. Ali, S. G. Abdu, M. Tahan, N.-A. Raship, A. S. Bakri, N. Nayan, Improvement of transparent conductive indium tin oxide based multilayer films on p-silicon through the inclusion of thin copper-aluminium metals interlayer, Thin Solid Films, vol. 738, no. 138959, 2021.

[16] A. K. Isiyaku, A. H. Ali, S. G. Abdu, M. Tahan, N.-A. Raship, A. S. Bakri, N. Nayan, Preparation of Sn doped In_2O_3 multilayer films on n-type Si with optoelectronics properties improved by using thin Al–Cu metals interlayer films, Mater. Sci. Semicond. Process., vol. 131, no. 105870, 2021.

[17] S. Li, W. Ma, X. Chen, K. Xie, Y. Li, X. He, X. Yang and Y. Lei, "Structure and antireflection properties of SiNWs arrays form mc-Si wafer through Ag-catalyzed chemical etching". Appl. Surf. Sci., vol. 369, pp. 232–240, 2016. doi:10.1016/j.apsusc.2016.02.028

[18] Z. R. Smith, R. L. Smith and S. D. Collins, "Mechanism of nanowire formation in metal assisted chemical etching". Electrochimica Acta., vol. 92, pp. 139–147, 2013.

[19] S. Nichkalo, A. Druzhinin, O. Ostapiv and M. Chekaylo, "Role of Ag-catalyst morphology and molarity of AgNO3 on the size control of Si nanowires produced by metal-assisted chemical etching". Mol. Cryst. Liq. Cryst., vol. 674, pp. 69–75, 2018.

[20] A. Abdulkadir, A. A. Aziz and M. Z. Pakhuruddin, "Effects of silver nanoparticles layer thickness towards properties of black silicon fabricated by metal assisted chemical etching for photovoltaics". SN Appl. Sci., vol. 2, no. 515, pp. 1-8, 2020.

[21] N. A. M. Noor, S. K. Mohamad, S.S . Hamil, M. Devarajan and M. Z. Pakhuruddin, "Effects of etching time towards broadband absorption enhancement in black silicon fabricated by silver-assisted chemical etching". Optik (Stuttg), vol. 176, pp. 586–592, 2019.

[22] R. G. Milazzo, G. D'Arrigo, C. Spinella, M. G. Grimaldi and E. Rimini, "Investigation of Ag-Assisted Chemical Etching on (100) and (111) Contiguous Silicon Surfaces". ECS J. Solid State Sci. Tech., vol. 2, pp. 405–412, 2013.

[23] N. A. M. Noor, S. K. Mohamad, S. S. Hamil and M. Z. Pakhuruddin, "Effects of annealing temperature towards surface morphological and optical properties of black silicon fabricated by silver-assisted chemical etching". Mat. Sci. Semicond. Proc., vol. 91, pp. 167–173, 2019.

[24] X. Li, K. Tao, D. Zhang, Z. Ghao, R. Jia, B. Wang, S. Jiang, Z. Ji and X. Liu, "Development of additive-assisted Ag-MACE for multicrystalline black Si solar cells". Electrochem. Comm., vol. 113, no. 106686, pp. 1-7, 2020.

[25] S H. Hu, Y S. Lin, T K. Tseng, S H. Su and L C. Wu, "Reducing light reflection by processing the surface of silicon solar cells". J. Mat. Sci: Mat. in Elect., vol. 6, pp. 1-7, 2020.

[26] A.K. Isiyaku, A.H. Ali, N. Nayan, "Structural optical and electrical properties of a transparent conductive ITO/Al – Ag/ITO multilayer contact, Beilstein J. Nanotech, vol. 11, pp. 695–702, 2020.

[27] A. K. Behera, R. N. Viswanath, C. Lakshmanan, T. Mathews and M. Kamruddin, "Synthesis of silicon nanowalls exhibiting excellent antireflectivity". Nano-Struct. & Nano-Obj., vol. 21, pp. 100424, pp. 1-7, 2020.

[28] C. Huo, J. Wang, H. Fu, X. Li, Y. Yang, H. Wang, A. Mateen, G. Farid and K. Q. Peng, "Metal-assisted chemical etching of silicon in oxidizing HF solutions: Origin, mechanism, development, and black silicon solar cell application". Adv. Funct. Mat., vol. 30, pp. 1–21, 2020.

[29] V. Aca-López, E. Quiroga-González, E. Gómez-Barojas, J. Światowska and J. A. Luna-López, "Effects of the doping level in the production of silicon nanowalls by metal assisted chemical etching". Mat. Sci. Semicond. Proc., vol. 118, no. 105206, pp. 1-9, 2020.

[30] K. Kim, B. Ki, H. Bong, K. Choi and J. Oh, "Ultralow optical and electrical losses via metal-assisted chemical etching of antireflective nanograss in conductive mesh electrodes". Adv. Opt. Mater., vol. 2000143, pp. 1–8, 2020.

[31] X. Yang, W. Zhang, J. Choi, H. Q. Ta, Y. Bai, L. Chen, M. Zhang, Y. Chen, Z. Guan, M. H. Rummeli and L. Liu, "Influence of bowl-like nanostructures on the efficiency and module power of black silicon solar cells". Sol. Energy, vol. 189, pp. 67–73, 2019.